Structural, Transport and Optical Properties of (La0.6Pr0.4)0.65Ca0.35MnO3 Nanocrystals: A Wide Band-gap Magnetic Semiconductor

Structural, Transport and Optical Properties of $(La_{0.6}Pr_{0.4})_{0.65}Ca_{0.35}MnO_3$ Nanocrystals: A Wide Band-gap Magnetic Semiconductor

Satyam Kumar,[§] G. D. Dwivedi,[‡] Shiv Kumar,[§] R. B. Mathur,[∥] U. Saxena,[†] A. K. Ghosh,[§] A. G. Joshi[$], H. D. Yang,[‡] and Sandip Chatterjee[*,⊥]

[§]Department of Physics, Banaras Hindu University, Varanasi-221005, India

[‡]Department of Physics, National Sun Yat-Sen University, Kaohsiung-80424, Taiwan

[∥]CSIR-National Physical Laboratory, Dr. K.S. Krishnan Road, New Delhi, India

[†]Department of Physics, Mahila Mahavidyalaya, Banaras Hindu University, Varanasi-221005, India

[$]CSIR-National Physical Laboratory, Dr. K.S. Krishnan Road, New Delhi, India

[⊥]Department of Physics, Indian Institute of Technology (Banaras Hindu University), Varanasi-221005, India

Abstract: $(La_{0.6}Pr_{0.4})_{0.65}Ca_{0.35}MnO_3$ system has been synthesized via sol-gel route at different sintering temperatures. Structural, transport and optical measurements have been done to investigate $(La_{0.6}Pr_{0.4})_{0.65}Ca_{0.35}MnO_3$ nanoparticles. Raman spectra show that Jahn-Teller distortion has been decreased due to the presence of Ca and Pr in A-site. Magnetic measurements provide Curie temperature around 200 K and saturation magnetization (M_S) about 3.43 μ_B/Mn at 5 K. X-ray photoemission spectroscopy study suggests that Mn exists with dual oxidation state (Mn^{3+} and Mn^{4+}). Resistivity measurements suggest that Charge-ordered state of Mn^{3+} and Mn^{4+}, which might be influenced by the presence of Pr, have enhanced insulating behavior in $(La_{0.6}Pr_{0.4})_{0.65}Ca_{0.35}MnO_3$. Band gap estimated from UV-Vis spectroscopy measurements comes in the range of wide band gap semiconductors ($\sim$ 3.5 eV), this makes it a potential candidate for device application.

*Corresponding author e-mail id: schatterji.app@iitbhu.ac.in

INTRODUCTION

Hole doped manganite systems have been generating curiosity among scientists and engineers from more than 60 years because of their unprecedentedand wide range of properties, e.g.; ferromagnetism, insulator-metal transition and colossal magnetoresistive properties. The physics behind all these properties are even more challenging and it had drawn attentions of theoreticians and experimentalists with almost equal authority.[1-11] Manganite materials have been used in different electronic devices such as magneto-tunable photocurrent devices, Resistive switching devices, Spin Hall-Magnetoresistive devices and many more.[12-18] The parent compound $LaMnO_3$ is known to be an antiferromagnetic insulator, while the divalent cation (Ca^{2+}, Sr^{2+} and Ba^{2+}) doping have induced paramagnetism with polaron type of conductivity at high temperatures and metallic ferromagnetism below the Curie temperature T_C. The origin of ferromagnetism has been attributed to the double-exchange interaction between the valence electronic states of Mn^{3+}-O^{-2}-Mn^{4+}.[19-21] Double-exchange mechanism along with the effect of lattice distortion believed to be responsible for the occurrence of Colossal Magnetoresistance (CMR).[22,23] As an outcome of the double-exchange interaction and the lattice distortion, a large spin splitting of the conduction band (majority and minority sub-bands) takes place in the ferromagnetic state.[8-11] Governed by Hund's rule, these sub-bands are separated by few electron-volts energy, which depends on A-site doping. The large spin splitting produces the half-metallic properties of the material, because at Fermi level, charge carriers with only one spin direction (up/down) are present whereas there is a gap in the density of states for the carriers with the other spin direction (down/up).

Hole doped manganite system in nano-range act in different way i.e., ferromagnetic ordering and metal-insulator transition are well separated from each other. Transport properties basically depend on boundary conditions. In nano-range, surface to volume ratio increases so boundary effect becomes more pronounced in transport properties. Due to more boundaries, charge carriers face much more scattering and as a result resistivity of the system increases. Whereas double exchange interaction between Mn^{3+} and Mn^{4+} is not affected with boundary conditions and therefore is not affected much in nano-phase.[24]

Magnetic properties of Ca doped $PrMnO_3$ ($Pr_{1-x}Ca_xMnO_3$) materials at low temperatures are governed by Mn^{3+}/Mn^{4+} ordering, intra- and inter-Mn exchange interactions and structural distortions produced by the Ca^{2+} cations. $PrMnO_3$ has an antiferromagnetic ground state. With Ca

doping, a ferromagnetic ground state develops for x = 0.2. Charge-ordering of the Mn- ions occurs over a wide range from 0.3<x<0.75 with an ordering temperature near 250 K.[25,26] $Pr_{0.65}Ca_{0.35}MnO_3$ shows insulating behavior in both the paramagnetic and ferromagnetic states because of charge-ordered state of Mn^{3+} and Mn^{4+}.[27]

Magnetic and transport properties of manganites have been studied with great interest and enthusiasm by scientists and will be continued to be studied in future because of the vast range of properties these systems possess which make them desirable from application point of view. However work has not been done concerning about their optical properties because these systems either show insulator (large band gap; typically>4 eV) behavior or metallic (no band gap) behavior which makes them less interesting for optical studies. In this manuscript, we have doped 40% Pr in La site of $La_{0.65}Ca_{0.35}MnO_3$ system which shows metallic ferromagnetic behavior below 260 K.[28] The idea behind the doping of Pr is that $Pr_{0.65}Ca_{0.35}MnO_3$ system shows ferromagnetic charge-ordered insulator behavior. We are expecting that with the doping of Pr, the semiconducting behavior will increase because of stabilization of charge-ordering, along with sustaining magnetic order of system. Along with strong magnetic moment, if we can induce semiconducting nature, these systems can be used as a better candidate to improve magnetic semiconducting devices. To realize this, we have used $La_{0.65}Ca_{0.35}MnO_3$ nanoparticles, which show better semiconducting nature along with ferromagnetic ordering as compared to its bulk counterpart. Additionally, doping of Pr may also increase its semiconducting behavior without disturbing magnetic ordering. We are using particularly 40% of Pr doping in La site because excess doping resulted in completely insulating phase, while doping less than 40% will decrease the band gap significantly,[10] both cases are not favorable for application purpose.

EXPERIMENTAL SECTION

$(La_{0.6}Pr_{0.4})_{0.65}Ca_{0.35}MnO_3$ samples were synthesized by using the sol–gel method. Analytical grade metal oxides Pr_6O_{11}, La_2O_3, and $CaCO_3$ powders were taken in stoichiometric proportions (0.39 mol: 0.26 mol: 0.35 mol) and dissolved in nitric acid (HNO_3) and thoroughly mixed for 30 minutes. The prepared solution of metal nitrates along with $Mn(NO_3)_3.4H_2O$ (1 mol) were mixed in aqueous solution of citric acid $[C_6H_8O_7]$ (99.5% purity) while stirring, to obtain a homogeneous precursor solution. Citric acid serves as fuel for the reaction. In this solution ethylene glycol was added drop wise while stirring. Citric acid, ethylene glycol and metal

nitrates were precisely taken in 4:3:1 molar ratio, respectively. The precursor solution was dried at 200° C for 12 hrs in oven to obtain xerogel and the swelled xerogel was kept at 300° C for 5 hrs to dry. After grinding the xerogel, powders were sintered at 600, 800, 1000° C for 5 hrs under air atmosphere to get $(La_{0.6}Pr_{0.4})_{0.65}Ca_{0.35}MnO_3$ nanoparticles.

Phase purity of as prepared $(La_{0.6}Pr_{0.4})_{0.65}Ca_{0.35}MnO_3$ samples were checked with Model: Philips X'pert ProX-ray diffractometer using CuK_α radiation (λ = 1.5406 Å). Transmission Electron Microscopy measurements were done with JEOL-2010 (Japan). Raman spectra were taken with a Reinshaw micro-Raman spectroscope in the range of 100 cm^{-1} to 1000 cm^{-1} using 514.5 nm Ar^+ laser as excitation source. Fourier Transform Infrared (FTIR) spectroscopy measurements were done with FTIR Spectrometer (Spectrum One, Perkin Elmer Instrument, USA) in the range of 4000–400 cm^{-1} with a resolution of 1 cm^{-1}. Magnetic measurements have been done using Superconducting Quantum Interference Device [Magnetic Property Measurement System (MPMS) XL-7, Quantum Design Inc.]. Room temperature X-ray photoemission spectroscopy measurements have been done using Perkin Elmer 1257 model, operating at an average base pressure of $\sim 5 \times 10^{-10}$ torr with a monochromatic AlK_α line at 1486.6 eV. Resistivity measurements were done via 2-probe method using Keithley 2400 Sourcemeter. The optical absorption spectra were measured in the range of 220–800 nm using UV-Vis spectrometer (SHIMADZU).

RESULTS AND DISCUSSION

Structural analysis.

X-ray diffraction patterns of $(La_{0.6}Pr_{0.4})_{0.65}Ca_{0.35}MnO_3$ sintered at 600 °C, 800 °C and 1000 °C have been shown in Figure 1. All the three samples are in single phase (without any secondary phase) and crystallize in orthorhombic Pbnm space group like their extreme parents $La_{0.65}Ca_{0.35}MnO_3$ and $Pr_{0.65}Ca_{0.35}MnO_3$. We have determined average crystallite size (D) of all the three samples sintered at 600 °C, 800 °C and 1000 °C from scherrer's formula;

$$D = \frac{0.9\,\lambda}{\beta cos\theta}$$

where $\lambda = 1.5406$ Å, wavelength of X-ray used, β is Full Width at half maximum (FWHM) of Bragg's reflection plane and θ is half of the angle of corresponding reflection plane. We have used most intense peak (110) as a reference plane to calculate the crystallite size, which comes about 25 nm, 27 nm and 29 nm respectively for the samples sintered at 600 °C, 800 °C and 1000 °C. We have also estimated the strain by using Williamson-Hall method.[29] The average strain values for different sizes of $(La_{0.6}Pr_{0.4})_{0.65}Ca_{0.35}MnO_3$ are given in Table 1.

To study the surface morphology and microstructure of $(La_{0.6}Pr_{0.4})_{0.65}Ca_{0.35}MnO_3$ nanocrystals, Low-resolution Transmission Electron Microscopy (TEM) measurements have been performed. Due to strong magnetic moment, particles are strongly agglomerated with each other to make irregular shapes and sizes, which makes it rather difficult to distinguish one from the other. Estimated average grain sizes of three samples sintered at 600 °C, 800 °C and 1000 °C comes about 36 nm, 38 nm and 42 nm respectively, which is consistent with the X-ray diffraction results of increase in crystallite sizes with increasing sintering temperature (Figure 2 (a, c and e)). Selected Area Electron Diffraction (SAED) image shows the increase of crystalline nature of $(La_{0.6}Pr_{0.4})_{0.65}Ca_{0.35}MnO_3$ system with increase of sintering temperature (Figure 2 (b, d and f)). $(La_{0.6}Pr_{0.4})_{0.65}Ca_{0.35}MnO_3$ sintered at 1000 °C shows much clearer and brighter bragg's spots than rest of the two systems sintered at 600 °C and 800 °C, which indicates better crystalline nature of this system. X-ray diffraction, Low-resolution TEM and SAED measurements have confirmed single crystalline nature of our samples with almost homogeneous distribution.

Raman Spectroscopy.

To investigate about crystal structure, lattice distortions and defects, Raman spectroscopy is considered to be most powerful non-destructive tool. We have doped 40% Pr in La- site of $La_{0.65}Ca_{0.35}MnO_3$ in order to achieve magnetic semiconductor materials. To study the effect of doping on the crystal structure and lattice distortions, we have done Raman spectra of $(La_{0.6}Pr_{0.4})_{0.65}Ca_{0.35}MnO_3$ nanoparticles sintered at 600 °C, 800 °C and 1000 °C which have been shown in Figure 3. In the orthorhombic rare-earth manganites, Raman modes become active due to deviations from the ideal cubic perovskite structure. Group theory analysis of the $LaMnO_3$ structure suggests 60 normal modes. Among all these 60 modes, only 24 modes are Raman active and remaining modes are Infrared (IR) active.[30]

$$\Gamma_{optical} = (7A_g + 7B_{1g} + 5B_{2g} + 5B_{3g})_{Raman} + (8A_u + 10B_{1u} + 8B_{2u} + 10B_{3u})_{IR}$$

These 24 Raman active modes can be divided into; 2 symmetric, 4 asymmetric stretching modes, 4 bending modes, 6 rotation/tilt modes of the octahedral and remaining 8 modes are associated with the motion of A-site (La/Pr/Ca) cations. All these Raman modes becomes active because of 4 fundamental distortions from the ideal perovskite structure, namely, rotations of MnO_6 octahedra around the cubic $[001]_c$ and $[110]_c$ axes, Jahn-Teller distortion, and A-site (La/Pr/Ca) shift from its position in the ideal perovskite lattice. Raman spectra of $(La_{0.6}Pr_{0.4})_{0.65}Ca_{0.35}MnO_3$ sintered at 600 °C, 800 °C and 1000 °C do not show any phase changes due to change in sintering temperature (Figure 4). We have observed 3 distinct Raman modes in 200-800 cm^{-1} range; first, around 230 cm^{-1}, second around 500 cm^{-1} and third around 680 cm^{-1}. Raman mode around 680 cm^{-1} assigned as $B_{2g}(1)$ is related to the symmetric stretching vibration of Oxygen in MnO_6 octahedra. However, a very broad Raman mode around 500 cm^{-1} can be divided in two distinct modes namely; 460 cm^{-1}($A_g(1)$) and 520 cm^{-1} ($B_{2g}(2)$) related to Jahn-Teller type asymmetric stretching mode and symmetric bending modes of MnO_6 octahedra, respectively. Dediu et al[31] has reported that $Pr_{0.65}Ca_{0.35}MnO_3$ shows no variation in Raman spectra above charge-ordered transition temperature (T_{CO}), while below T_{CO}, Raman mode near 475 cm^{-1} has been divided into two modes $A_g(1)$ and $B_{2g}(2)$. In our case, due to the presence of Ca and Pr in A-site, the Jahn-Teller distortion at room temperature further suppressed and the Raman mode related to this becomes relatively less prominent,[29] consequently, the modes around 500 cm^{-1} are not quite distinguishable. Raman mode around 230 cm^{-1} assigned as $A_g(2)$ is related to tilting of MnO_6 octahedra. Raman modes observed in the range of 100-200 cm^{-1} are predominantly because of the vibrations of A-site cations.

Fourier Transform Infrared Spectroscopy.

To get the information about the molecular and functional species present on the surface and to further investigate lattice vibration present in our system, we have used Fourier Transform Infrared (FTIR) Spectroscopy. FTIR measurements of $(La_{0.6}Pr_{0.4})_{0.65}Ca_{0.35}MnO_3$ sintered at 600 °C, 800 °C and 1000 °C have been shown in Figure 4. In finger-print region, the band around 600 cm^{-1} corresponds to characteristic Mn-O bond. This confirms that each sample strongly contains the Mn-O bond and the change in bond length of Mn-O-Mn, because of the internal motion, is responsible for the band formation. Stretching vibration is responsible for the change

in Mn-O-Mn length, while the bending vibration involves the change of Mn-O-Mn bond angle. The peaks at 1400 and 1630 cm^{-1} corresponds to asymmetric stretching vibrations of C=C bond and symmetric stretching of C=O bond in citrate (which formed in the solution and may present on the surface of nano-crystals).

Magnetic Properties.

To investigate the magnetic properties of $(La_{0.6}Pr_{0.4})_{0.65}Ca_{0.35}MnO_3$ nanoparticles sintered at 600 °C, 800 °C and 1000 °C, we have performed temperature dependent field cooled magnetization measurement (M-T) from 300 K to 5 K at 100 Oe magnetic field (figure 5). M-T measurement of all the samples show that ferromagnetic transition occurs around 200 K and particle size is not showing any significant effect on Curie temperature, but it is affecting the magnetic moment considerably. $(La_{0.6}Pr_{0.4})_{0.65}Ca_{0.35}MnO_3$ sintered at 600 °C, 800 °C and 1000 °C are showing magnetic moments 6.58 emu/gm, 8.56 emu/gm and 7.53 emu/gm respectively at 5 K. At low magnetic field, $(La_{0.6}Pr_{0.4})_{0.65}Ca_{0.35}MnO_3$ sintered at 800 °C is showing higher magnetization value than $(La_{0.6}Pr_{0.4})_{0.65}Ca_{0.35}MnO_3$ sintered at 1000 °C, but at higher field $(La_{0.6}Pr_{0.4})_{0.65}Ca_{0.35}MnO_3$ sintered at 1000 °C shows higher saturated magnetic moment. Calculated saturation magnetization (M$_s$) of $(La_{0.6}Pr_{0.4})_{0.65}Ca_{0.35}MnO_3$ comes around 3.65 μ_B/Mn (with 65% Mn^{3+} and 35% Mn^{4+}). M-H measurements at 5 K shows 5 T of magnetic field gives saturation magnetization of 2.49 μ_B/Mn, 3.03 μ_B/Mn and 3.43 μ_B/Mn for $(La_{0.6}Pr_{0.4})_{0.65}Ca_{0.35}MnO_3$ sintered at 600 °C, 800 °C and 1000 °C , respectively (inset figure 5). Magnetic moment observed for $(La_{0.6}Pr_{0.4})_{0.65}Ca_{0.35}MnO_3$ sintered at 1000 °C is very close to calculated magnetic moment 3.65 μ_B/Mn. This shows, with increasing particle size magnetic response increases consistently and coming close towards magnetic moment of bulk $(La_{0.6}Pr_{0.4})_{0.65}Ca_{0.35}MnO_3$. This confirms the strong ferromagnetic character of our samples below 200 K. Ferromagnetic behavior of a similar $(La_{0.7}Pr_{0.3})_{0.65}Ca_{0.35}MnO_3$ have been reported earlier,[32] which is consistent with our result.

X-ray Photoemission spectroscopy.

X-ray photoemission spectroscopy (XPS) study have been done to investigate the chemical state of $(La_{0.6}Pr_{0.4})_{0.65}Ca_{0.35}MnO_3$ nanoparticles sintered at 600 °C, 800 °C and 1000 °C (figure 6). Survey scan of $(La_{0.6}Pr_{0.4})_{0.65}Ca_{0.35}MnO_3$ sintered at 600 °C, 800 °C and 1000 °C confirms the presence of La, Pr, Ca, Mn and O on the surface (figure 6(a)). High resolution XPS

core level spectra of Ca2p, Mn2p, O1s region have been shown in figure 6 (b), (c) and (d) respectively. In Ca2p region, peaks observed at 345.5 eV and 349 eV have been assigned as Ca2p$_{3/2}$ and Ca2p$_{1/2}$. The spin-orbit splitting energy is 3.5 eV, which indicates that the Ca exist in +2 oxidation state. In O1s region, two peaks at 528.7 eV and 530.7 eV are attributed to the contribution of the crystal lattice oxygen and adsorbed oxygen, respectively. The adsorbed oxygen has tendency to tie up with oxygen vacancies (V$_o$). In Mn2p region, the two peaks are located at 641.5 and 653 eV, which belong to Mn2p$_{3/2}$ and Mn2p$_{1/2}$, respectively. The peaks of Mn2p$_{3/2}$ and Mn2p$_{1/2}$ can be deconvoluted into two peaks each. The deconvoluted peaks of Mn2p region for $(La_{0.6}Pr_{0.4})_{0.65}Ca_{0.35}MnO_3$ sintered at 600 °C have been shown as a representative in figure 6(e). The deconvoluted peaks of Mn2p$_{3/2}$ at 640.88eV and 642.85 eV (and Mn2p$_{1/2}$ at 652.48 eV and 654.54 eV) represent Mn^{3+} and Mn^{4+}, respectively. This confirms that Mn exist in two oxidation state (+3 and +4), which participate in the double exchange interaction to give ferromagnetic ordering in the system. Valence band spectra have been shown in figure 6(f) for discussed nanoparticles. Two most intense peaks around 2.7 eV and 6.2 eV are due to the strong hybridization of Mn3d(t$_{2g}$) and O2p states. A weak emission near Fermi level have been detected which belongs to Mn3d(e$_g$) states. A similar kind of features had been reported earlier in manganite materials,[33,34] which supports our result.

Resistivity Measurement.

$La_{0.65}Ca_{0.35}MnO_3$ shows insulator-metal transition around 260 K[28] but $Pr_{0.65}Ca_{0.35}MnO_3$ shows charge ordered type insulating behavior down to low temperature side.[35] The primary reason behind the formation of Charge-ordered state in $Pr_{0.65}Ca_{0.35}MnO_3$ is competition between double exchange and super exchange among the core spins of Mn and the Coulomb interaction between electrons of different orbitals of the same Mn-site.[36,37] Figure 7 shows the variation of resistivity (ρ) with respect to temperature for $(La_{0.6}Pr_{0.4})_{0.65}Ca_{0.35}MnO_3$ sintered at 600 °C, 800 °C and 1000 °C. $(La_{0.6}Pr_{0.4})_{0.65}Ca_{0.35}MnO_3$ system shows insulator type behavior at higher temperature side because of the development of charge-ordered states in nano-cyrstalline system due to the presence of ample amount of Pr in A-site and it is playing dominant role in transport behavior of the system at higher temperatures but at low temperature side, double exchange interaction becomes more dominant and system starts to behave as a metal. The insulator-metal transition temperature (T$_{IM}$) and resistivity (ρ) of nanoparticles depend on sintering temperature of the system and decreases with increase of sintering temperature. In other words, insulator-

metal transition temperature depends on the particle size of nano-crystals, as we have seen in X-ray diffraction analysis and low-resolution transmission electron microscopy analysis, particle size is increasing with increase in sintering temperature. Due to the increase in particle (grain) size, the effect of grain boundary reduces and consequently the charge carrier faces less scattering from grain boundaries. This factor also improves double exchange interaction mechanism and system starts to show metal-insulator transition at higher temperature and resistivity of the system also decreased significantly.

The resistivity of $(La_{0.6}Pr_{0.4})_{0.65}Ca_{0.35}MnO_3$ sintered at 600 °C, 800 °C and 1000 °C can be well fitted by $\rho = \rho_0 \exp(E_a/k_B T)$ for nearest-neighbour hopping of small polarons [Fig.8] where k_B is the Boltzmann's constant and Ea is the activation energy. The activation energy (E_a) for the samples has been calculated using small polaron theory, and values are given in Table 2. With increasing the sintering temperature, the resistivity and E_a both decrease. The linear fit shows that thermally activated band conduction is the dominant mechanism at high-temperature region. The deviation from the linear fit indicates that thermal activation mechanism is not valid at the low-temperature region. The variable-range-hopping (VRH) conduction of polarons has been found to dominate in this temperature region. The conduction mechanism due to the variable range hopping of polaron at low temperature can be described by the Mott's equation[38-40] $\rho(T) = \rho_0 \exp[T_0/T]^{1/4}$ where ρ_0 and T_0 are constants and are given by $\rho_0 = \{[8\pi\alpha k_B T/N(E_F)]^{1/2}\}/(3e^2 v_{ph})$ and $T_0 = 18\alpha^3/[k_B N(E_F)]$ where v_{ph} (~10^{13} s−1) is the phonon frequency at Debye temperature, $N(E_F)$ is the density of localized electron states at the Fermi level, and α is the inverse localization length. Using above equations, a linear plot is expected from $\ln(\rho T^{-1/2})$ versus $(1/T)^{1/4}$ for VRH conduction. The linear fit of $\ln(\rho T^{-1/2})$ versus $(1/T)^{1/4}$ plot (see inset fig:8) indicates that VRH is the dominant mechanism of conduction below a certain temperature T_h. The T_h values are 165 K, 147K and 140K respectively, for 600 °C, 800 °C and 1000 °C sintered samples. The average hopping distance (R) and average hopping energy (E_h) at 150 K have been calculated from $R = [9/8\pi\alpha k_B T N(E_F)]^{1/4}$ and $E_h = 3/[4\pi R^3 N(E_F)]$. Other conditions for VRH conduction[41] are that the value of $\alpha R > 1$ and that $E_h > k_B T$. Both of these conditions are satisfied in all the studied samples (See Table2). It is not possible that the variation of particle sizes can change the $N(E_F)$ which in effect can account for the large decrease of T_0. But, the decrease of T_0 may indicate the increase of localization length α^{-1} which leads to electronic delocalization.

Ultraviolet-VisibleSpectroscopy.

To investigate the optical absorbance and evaluate optical band gap of $(La_{0.6}Pr_{0.4})_{0.65}Ca_{0.35}MnO_3$ we have studied the Ultraviolet-Visible (UV-Vis) spectroscopy. UV-Vis spectroscopy measurements have been done for $(La_{0.6}Pr_{0.4})_{0.65}Ca_{0.35}MnO_3$ sintered at 600 °C, 800 °C and 1000 °C (Figure 9). UV-Vis spectra of all the three samples can be divided into three parts (i) a sharp absorption edge around 308 nm (ultraviolet region) (ii) exponential decay region near absorption edge (ultraviolet to visible region) and (iii) a long smooth extended region (visible to infra-red region). The optical absorption edge have been analyzed by,[42]

$$\alpha h\nu \propto (h\nu - E_g)^n$$

Where n is equal to ½ and 2 for direct and indirect transitions respectively, while absorption coefficient 'α' can be calculated from equation,

$$\alpha(\nu) = 2.303 \times (^A/_d)$$

where 'A' is the optical absorbance and 'd' is thickness of the sample. The variation of $(\alpha h\nu)^2$ with photon energy $h\nu$ for $(La_{0.6}Pr_{0.4})_{0.65}Ca_{0.35}MnO_3$ sintered at 600 °C, 800 °C and 1000 °C have been plotted in Figure 10. $(\alpha h\nu)^2$ varies linearly for very wide range of photon energy ($h\nu$), which suggest direct type of transitions in these systems. The intercepts of these plots on the energy axis give the energy band gaps of the systems. Direct band gaps of $(La_{0.6}Pr_{0.4})_{0.65}Ca_{0.35}MnO_3$ sintered at 600 °C, 800 °C and 1000 °C determined from these plots are 3.52 eV, 3.46 eV and 3.42 eV respectively. The decrease in band gap (red-shift) with increasing sintering temperature can be attributed to increased particle sizes which have been related to the increased metallic behavior in resistivity analysis. The observed band gaps of these systems come in the range of wide band gap semiconductors and these values are even more than the band gap of ZnO (3.37 eV) and GaN (3.44 eV).[43-45] Additionally, these systems show much better magnetic ordering and magnetic moment[46] than any known diluted magnetic semiconductors, which might prove significant in the applications as magnetic semiconductors.

The absorption coefficient near the band edge decays exponentially with photon energy (Figure 9) and this dependence can be written as follows,[47]

$$\alpha = \alpha_0 \exp(\frac{h\nu}{E_u})$$

where 'α_0' is a constant and E_u is Urbach energy defined as the width of the localized states (related to the amorphous state) present in the forbidden gap. This exponential dependence on photon energy may arise due to the random fluctuations associated with the small structural disorder present within the system.

CONCLUSION

X-ray diffraction, low-resolution TEM, SAED and X-ray Photoemission Spectroscopy (XPS) measurements have been done to confirm the phase formation, crystal quality and chemical constituents of our $(La_{0.6}Pr_{0.4})_{0.65}Ca_{0.35}MnO_3$ systems. Crystallite size and grain size calculated from XRD and TEM respectively, confirms nano-crystalline structure of our systems. SAED images show, system becomes more crystalline with increasing sintering temperature. Raman spectra of $(La_{0.6}Pr_{0.4})_{0.65}Ca_{0.35}MnO_3$ show typical vibration modes of perovskite structures. Raman study confirms the stretching ($B_{2g}(1)$), bending ($B_{2g}(2)$) and tilting ($A_g(2)$) modes of Oxygen in MnO_6 octahedra which play a significant role in structural distortion along with Jahn-Teller distortion ($A_g(1)$) mode, but due to the presence of Pr and Ca in A-site, Jahn-Teller distortion decreases which is evident from the reduction of $A_g(1)$ mode. FTIR measurements further confirms the presence of characteristic Mn-O stretching vibration mode near 600 cm^{-1}, which is responsible for the structural distortion, magnetic and transport properties of this system. Magnetization measurement shows the ferromagnetic ordering occurs around 200 K and system shows saturation magnetization of 3.43 μ_B/Mn, which is very close to the calculated value of bulk sample. XPS measurement confirms that Mn exist in dual oxidation state (Mn^{3+} and Mn^{4+}), which contributes in double exchange interaction and ferromagnetic ordering. Valence band spectra shows two intense peaks around 2.7 eV and 6.2 eV which is due to strong Mn3d(t_{2g})-O2p hybridization. Resistivity measurement shows that due to doping of Pr in A-site, system started to behave like charge ordered insulator and insulator-metal transition decreases up to 98 K. With increase of particle size (by increasing sintering temperature) this insulator-metal transition temperature improves to higher temperature side. Band gap estimated from UV-Vis measurement comes in wide band gap semiconductor range (~ 3.5 eV) which is higher than ZnO(3.37 eV) and GaN (3.44 eV) systems. We believe that with wide band gap and

strong magnetic properties, $(La_{0.6}Pr_{0.4})_{0.65}Ca_{0.35}MnO_3$ system will certainly prove a potential candidate for magnetic semiconductor device application.

REFERENCES

1 G. Jonker and J. van Santen, *Physica (Amsterdam)*,1950, **16**, 337.

2 E. O. Wollan and W. C. Koehier, *Phys. Rev.*,1955, **100**, 545.

3 R. von Helmolt, J. Weeker, B. Hopzapfel, L. Schulz, and K. Samwer,*Phys. Rev. Lett.*, 1993, **71**, 2331.

4 S. Jin, T. H. Teifel, M. McCormack, R. A. Fastnacht, R. Ramesh and L.H. Chen, *Science*, 1994, **264**, 413.

5 J. Vogier, *Physica (Amsterdam)*,1954, **20**,48.

6 P. Schiffer, A. P. Raniirez, W. Bao and S. W. Cheong, *Phys. Rev. Lett.*, 1995, **75**, 3336.

7 A. P. Ramirez, *J. Phys.: Condens. Matter.*, 1997,**9**, 8171.

8 J. M. Coey, M. Viret and S. von Molnar, *Adv. Phys.*, 1999, **48**, 167.

9 M. B. Salamon and M. Jaime, *Rev. Mod. Phys.*, 2001, **73**, 583.

10 E. Dagotto, T. Hotta and A. Moreo, *Phys. Rep.*, 2001, **344**, 1.

11 M. Ziese, *Rep. Prog. Phys.*, 2002, **65**, 143.

12 Z. G. Sheng, M. Nakamura, W. Koshibae, T. Makino, Y. Tokura and M. Kawasaki, *Nature Commun.*, 2014, **5**, 4584.

13 S. N. Jammalamadaka, J. Vanacken and V. V. Moshchalkov, *Appl. Phys. Lett.*, 2014, **105**, 033505.

14 H. Nakayama, M. Althammer, Y.-T. Chen, K. Uchida,Y. Kajiwara, D. Kikuchi, T. Ohtani, S. Geprägs, M. Opel, S. Takahashi, R. Gross, G. E. W. Bauer, S. T. B. Goennenwein, and E. Saitoh, *Phys., Rev. Lett.*, 2013, **110**, 206601.

15 H. Boschker, J. Kautz, E. P. Houwman, W. Siemons, D. H. A. Blank, M. Huijben, G. Koster, A. Vailionis and G. Rijnders, *Phys. Rev. Lett.* 2012, **109**, 157207.

16 M. Nakamura, Y. Ogimoto, H. Tamaru, M. Izumi and K. Miyano, *Appl. Phys. Lett.* 2005, **86**, 182504.

17 Y. Ogimoto, N.Takubo, M. Nakamura, H. Tamaru, M. Izumi and K.Miyano, *Appl. Phys. Lett.* 2005, **86**, 112513.

18 M. Minohara, Y. Furukawa, R. Yasuhara, H. Kumigashira and M. Oshima, *Appl. Phys. Lett.* 2009, **94**, 242106.

19 C. Zener, *Phys. Rev.*, 1951, **81**, 440.

20 P. W. Anderson and H Hasegawa, *Phys. Rev.*, 1955, **100**, 675.

21 J. Goodenough, *Phys. Rev.*, 1955, **100**, 564.

22 A. J. Millis, P. B. Littlewood and B. I. Shraiman, *Phys. Rev. Lett.*, 1995, **74**, 5144.

23 A. J. Millis, B. I. Shraiman and R. Mueller, *Phys. Rev. Lett.*, 1996, **77**, 175.

24 Anurag Gaur and G. D. Varma, *J. Phys.: Condens. Matter*, 2006, **18**, 8837.

25 E. Pollert, S. Krupicka and E. Kuzmicova, *J. Phys. Chem. Solids*, 1982, **43**, 1137.

26 Z. Jirak, S. Krupicka, Z. Somsa, M. Dlouha and S. Vratislav, *J. Magn. Magn. Mater.*, 1985, **53**, 153.

27 Y. Tomioka, A. Asamitsu, H. Kuwahara, Y. Morimoto and Y. Tokura, *Phys. Rev. B*, 1996, **53**, R1689.

28 B. Lorenz, A. K. Heilman, Y. S. Wang, Y. Y. Xue, C. W. Chu, G. Zhang and J. P. Franck, *Phys. Rev. B*, 2001, **63**, 144405.

29 G. K. Williamson and W. H. Hall, *Acta Metall.,* 1953,**1,**22.

30 J. Agostinho Moreira, A. Almeida, W. S. Ferreira, J. E. Araújo, A. M. Pereira, and M. R. Chaves, J. Kreisel, S. M. F. Vilela and P. B. Tavares, *Phys. Rev. B*, 2010, **81**, 054447.

31 V. Dediu, C. Ferdeghini, F. C. Matacotta, P. Nozar and G. Ruani, *Phys. Rev. Lett.*, 2000, **84**, 4489.

32 H. Sakaiand Y. Tokura, *Appl. Phys. Lett.*, 2008, **92**, 102514.

33 A. Santoni, G. Speranza, M. R. Mancini, F. Padella, L. Petrucci and S. Casadio, *J. Phys.: Condens. Matter*, 1999, **11**,3387.

34 A.Kowalczyk, J. Baszynˊ ski, A.Szajek, A. Sˊ lebarskiand T.Tolinˊ ski, *J. Phys.: Condens. Matter*, 2001, **13**,5519.

35 A. Biswas and I. Das, *Phys. Rev. B*, 2006, **74**, 172405.

36 J. van den Brink and D. Khomskii, *Phys. Rev. Lett.*, 1999, **82**, 1016.

37 J. van den Brink, G. Khaliullin and D. Khomskii, *Phys. Rev. Lett.*, 1999,**83**, 5118.

38 N. F. Mott,*J. Non-Cryst. Solids*,1968,**1,** 1.

39 N. Sharma, S. Granville, S. C. Kashyap and J.-Ph. Ansermet, *Phys. Rev. B*,2010,**82,** 125211

40 G. D. Dwivedi, K. F. Tseng, C. L. Chan, P. Shahi, J. Lourembam, B. Chatterjee,A. K. Ghosh, H. D. Yang, and S. Chatterjee *Phys. Rev. B*, 2010,**82,** 134428.

41 N. F. Mott and E. A. Davis, *Electronics Process in Non-Crystalline Materials*; Clarendon: Oxford, U.K., **1979**

42 N. F. Mott and R. W. Gurney, *Electronic Processes in Ionic Crystals,* Oxford Univ. Press, London,**1940.**

43 A. Mang, K. Reimann and St. Rübenacke, *Solid State Commun.,* 1995,**94,** 251.

44 O. Madelung, *Semiconductors-Basic Data 2nd Revised Edition (Berlin: Springer)*, **1996**.

45 S. Kumar, S. Chatterjee, K. K. Chattopadhyay, and A. K. Ghosh*J. Phys. Chem. C,*2012,**116,** 16700.

46 S.Taran, S. Chatterjee and B.K.Chaudhuri, *Phys. Rev. B,*2004,**69,** 184413

47 F. Urbach, *Phys Rev.*,1953,**92,**1324.

Table:1: Particle sizes estimated from X-ray diffraction and TEM and average strain estimated using Williamson-Hall method

Samples	Average Strain (Estimated using Williamson-Hall method)	Particle size (nm) (Estimated from XRD data)	Particle Size(nm) (Estimated from TEM
$(La_{0.6}Pr_{0.4})_{0.65}Ca_{0.35}MnO_3$ sintered at 600 °C	1.58×10^{-3}	25	36
$(La_{0.6}Pr_{0.4})_{0.65}Ca_{0.35}MnO_3$ sintered at 800 °C	2.75×10^{-3}	27	38
$(La_{0.6}Pr_{0.4})_{0.65}Ca_{0.35}MnO_3$ sintered at 1000 °C	4.92×10^{-3}	29	42

Table:2: Values of Various Parameters of Variable-Range-Hopping Mechanism of $(La_{0.6}Pr_{0.4})_{0.65}Ca_{0.35}MnO_3$ and activation energy from small polaron theory

Samples	T_0 (K)	α (cm−1) (inverse localization length)	R (cm) (average hopping distance)	Activation Energy(eV) (From SPT)	Hopping Energy E_h(eV) (From VRH)
$(La_{0.6}Pr_{0.4})_{0.65}Ca_{0.35}MnO_3$ sintered at 600 °C	3.495×10^6	2.918×10^4	7.110×10^{-4}	0.0706	3.37×10^{-6}
$(La_{0.6}Pr_{0.4})_{0.65}Ca_{0.35}MnO_3$ sintered at 800 °C	6.141×10^6	2.815×10^6	1.971×10^{-6}	0.1015	3.80×10^{-4}
$(La_{0.6}Pr_{0.4})_{0.65}Ca_{0.35}MnO_3$ sintered at 1000 °C	1.000×10^7	1.361×10^9	9.919×10^{-8}	0.1146	4.39×10^{-4}

Figure Caption:

Figure 1. X-ray diffraction pattern of $(La_{0.6}Pr_{0.4})_{0.65}Ca_{0.35}MnO_3$ nanoparticles sintered at 600 °C, 800 °Cand 1000 °C.

Figure 2. Low-resolution Transmission Electron Micrographs and their correspondingSelected Area Electron Diffraction images of $(La_{0.6}Pr_{0.4})_{0.65}Ca_{0.35}MnO_3$ nanoparticles sintered at 600 °C (a,b), 800 °C (c,d) and 1000 °C (e,f) respectively.

Figure 3. Raman Spectra of $(La_{0.6}Pr_{0.4})_{0.65}Ca_{0.35}MnO_3$ nanoparticles sintered at 600 °C, 800 °C and 1000 °C.

Figure 4. Fourier Transform Infrared Spectroscopy of $(La_{0.6}Pr_{0.4})_{0.65}Ca_{0.35}MnO_3$ nanoparticles sintered at 600 °C, 800 °C and 1000 °C.

Figure 5. Field cooled temperature dependent magnetization measurements of $(La_{0.6}Pr_{0.4})_{0.65}Ca_{0.35}MnO_3$ nanoparticles sintered at 600 °C, 800 °C and 1000 °C at 100 Oe magnetic field down to 5 K. Inset figure shows the M-H hysteresis loop up to 5T magnetic field at 5 K.

Figure 6. (a) Survey scan X-ray Photoemission spectroscopy (XPS) have been done for $(La_{0.6}Pr_{0.4})_{0.65}Ca_{0.35}MnO_3$ nanoparticles sintered at 600 °C, 800 °C and 1000 °C. High resolution core level XPS of (b) Ca2p region, (c) O1s region, (d) Mn2p region have been shown for $(La_{0.6}Pr_{0.4})_{0.65}Ca_{0.35}MnO_3$ nanoparticles sintered at 600 °C, 800 °C and 1000 °C. (e) Deconvoluted peaks of Mn2p region for $(La_{0.6}Pr_{0.4})_{0.65}Ca_{0.35}MnO_3$ nanoparticles sintered at 600 °C have been shown as a representative. (f) Valence band spectra of $(La_{0.6}Pr_{0.4})_{0.65}Ca_{0.35}MnO_3$ nanoparticles sintered at 600 °C, 800 °C and 1000 °C.

Figure 7. Variation of resistivity with temperature of $(La_{0.6}Pr_{0.4})_{0.65}Ca_{0.35}MnO_3$ nanoparticles sintered at 600 °C, 800 °C and 1000 °C.

Figure 8. Variation of $\ln\rho$ as function of 1000/Tfor $(La_{0.6}Pr_{0.4})_{0.65}Ca_{0.35}MnO_3$ nanoparticles sintered at 600 °C, 800 °C and 1000 °C at low temperature region (respectively, for T>164K, 147K and 140K). Inset: $\ln(\rho T^{-1/2})$ vs. $T^{-1/4}$ at lower temperature region (respectively, forT<164K, 147K and 140K and above the metal-semiconductor transition temperature). The linear fit indicates the variable range hopping conduction is active in this temperature range.

Figure 9. Ultraviolet-Visible spectra of $(La_{0.6}Pr_{0.4})_{0.65}Ca_{0.35}MnO_3$ nanoparticles sintered at 600 °C, 800 °C and 1000 °C.

Figure 10. Variation of $(\alpha h\nu)^2$ versus photon energy 'hν' plot for $(La_{0.6}Pr_{0.4})_{0.65}Ca_{0.35}MnO_3$ nanoparticles sintered at 600 °C, 800 °C and 1000 °C.
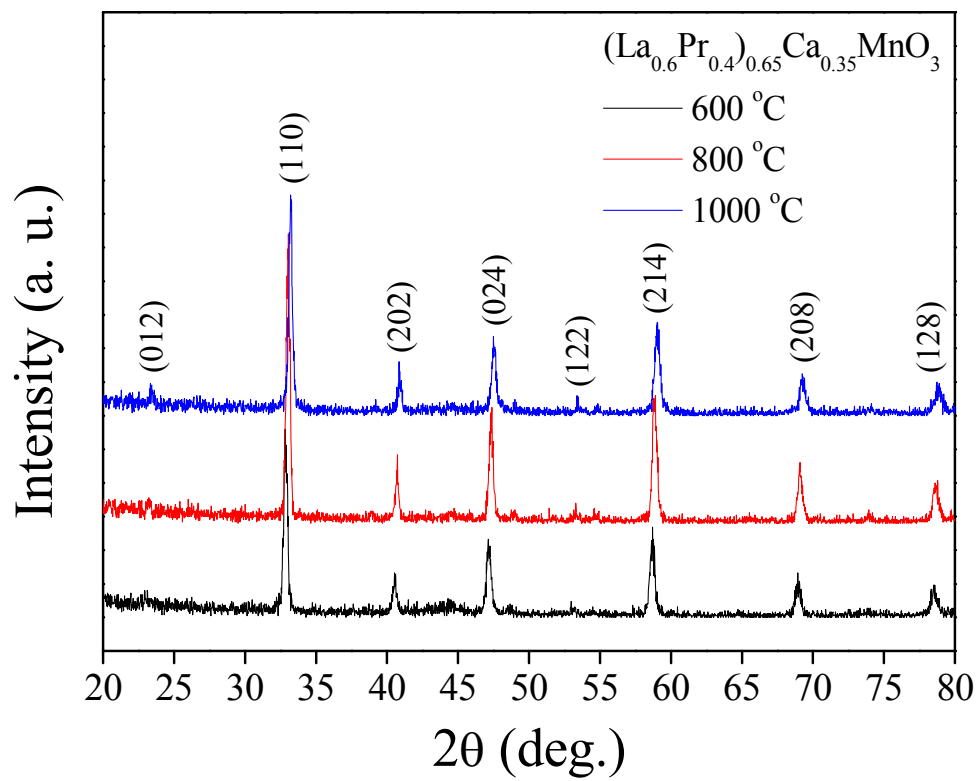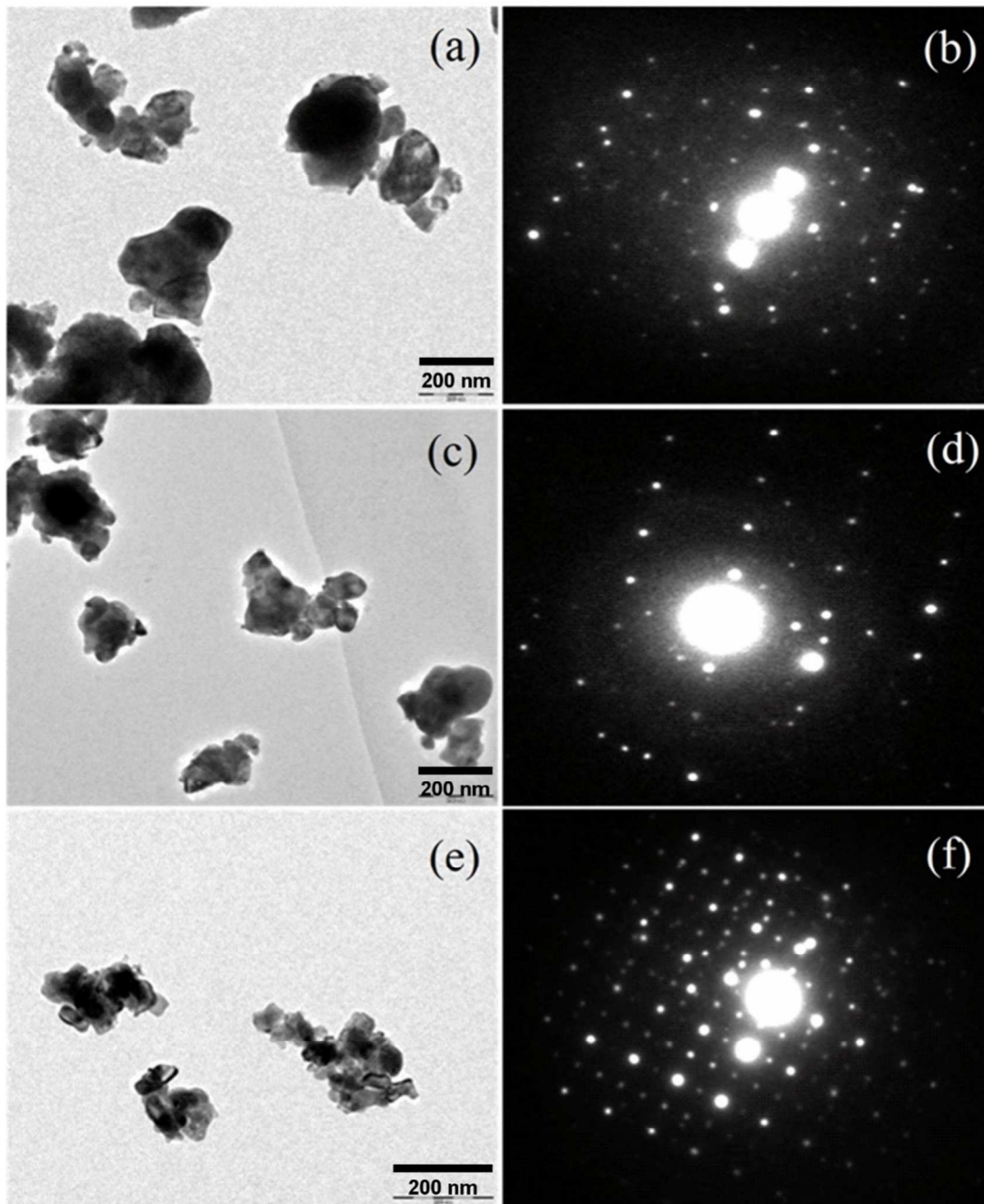
Figure 1

Figure 2
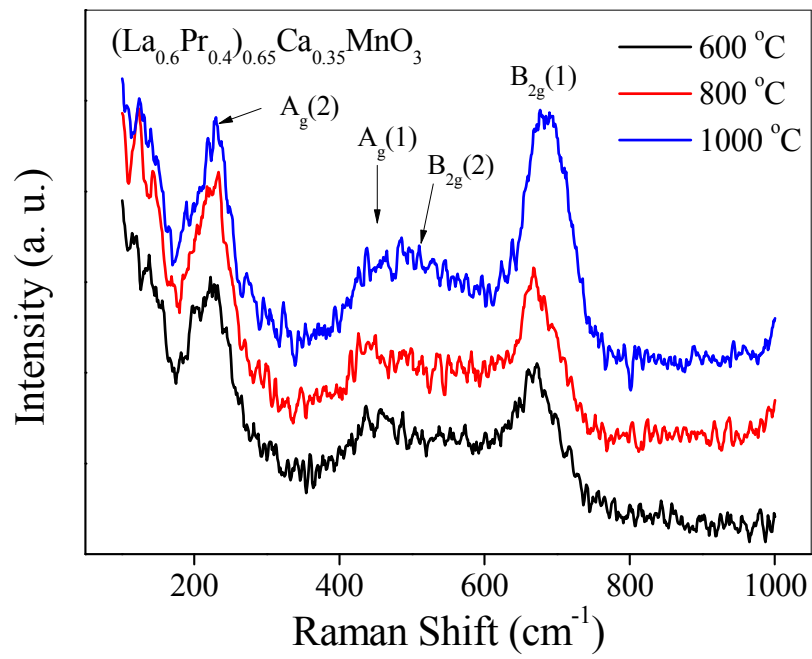
Figure 3
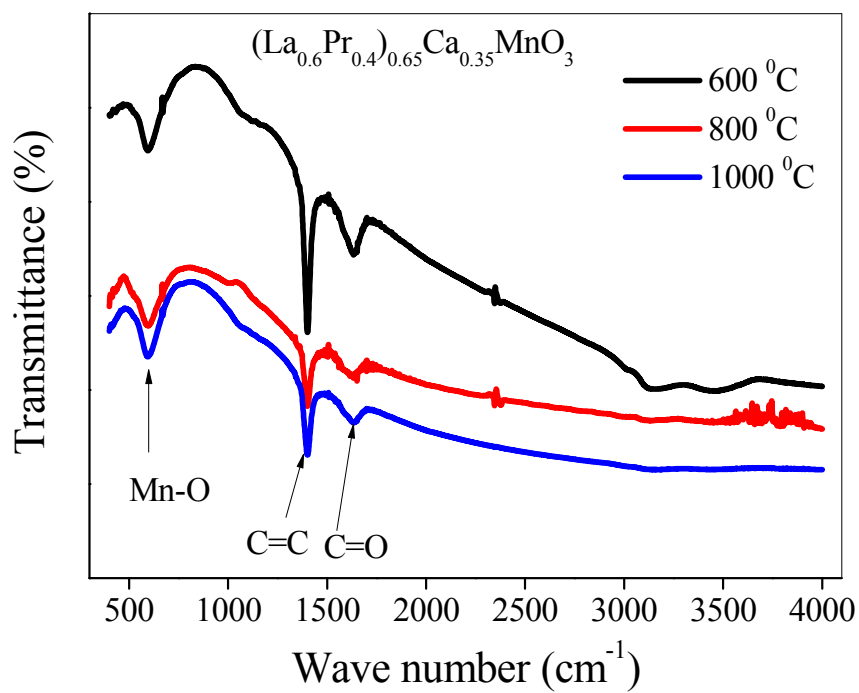
Figure 4
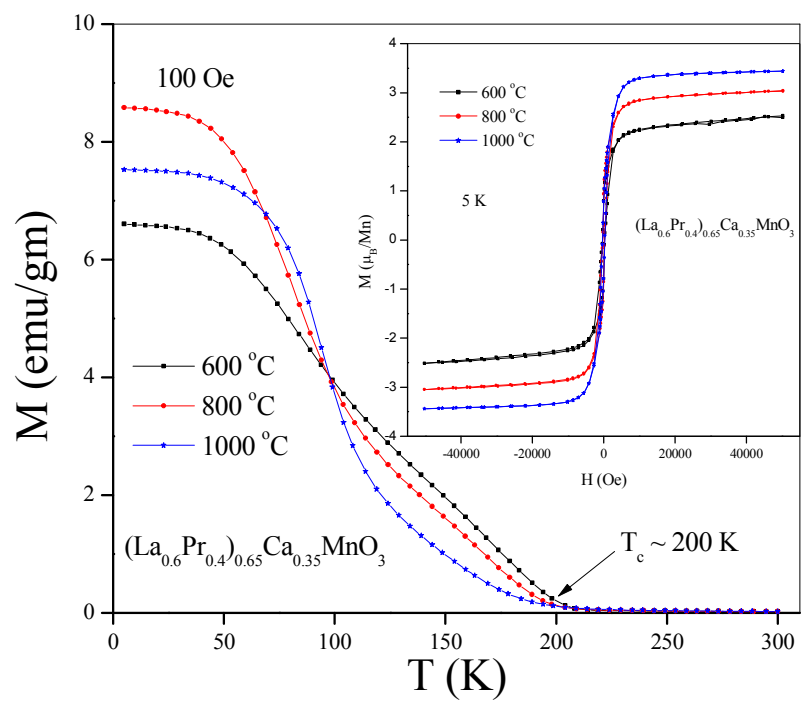
Figure 5
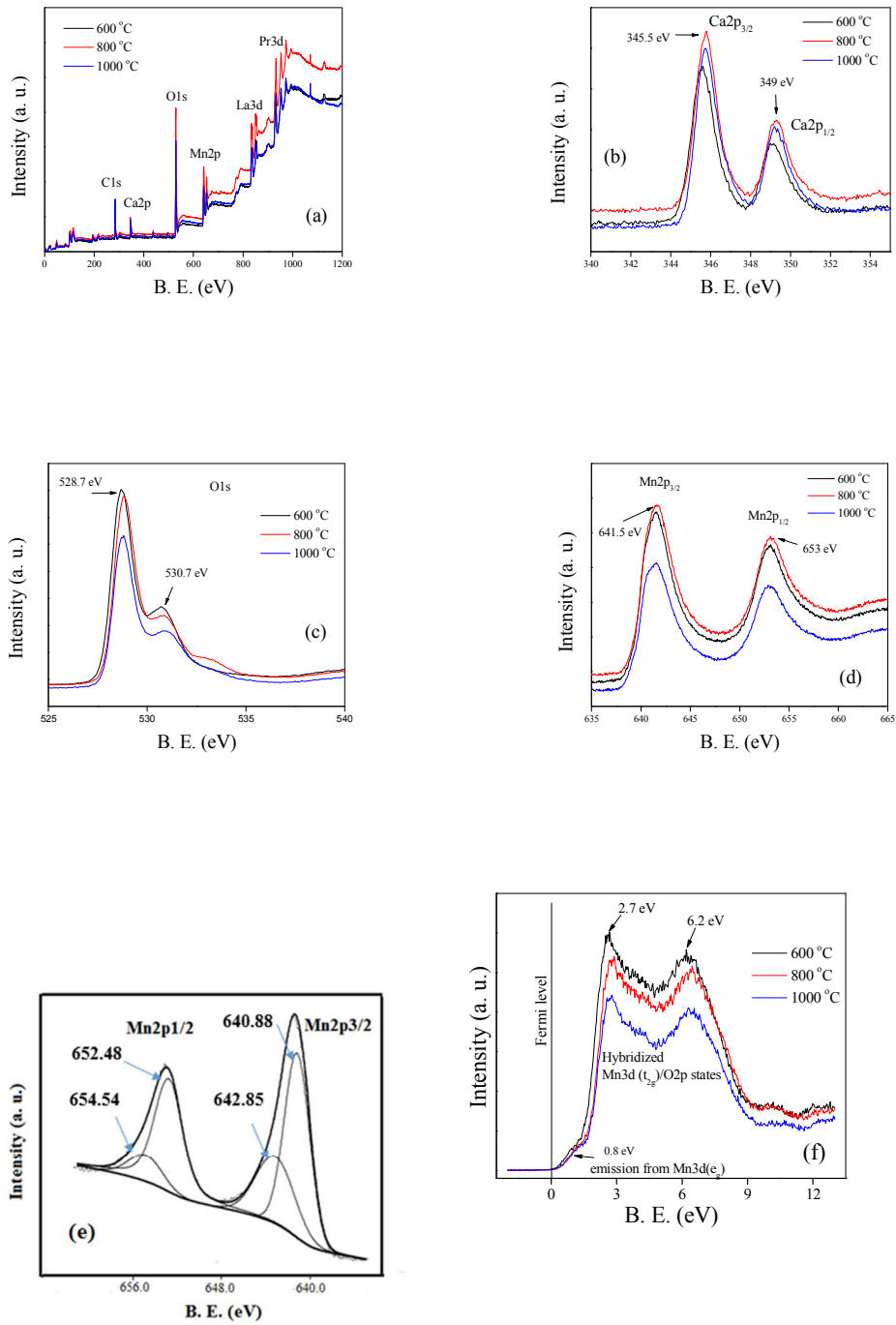
Figure 6
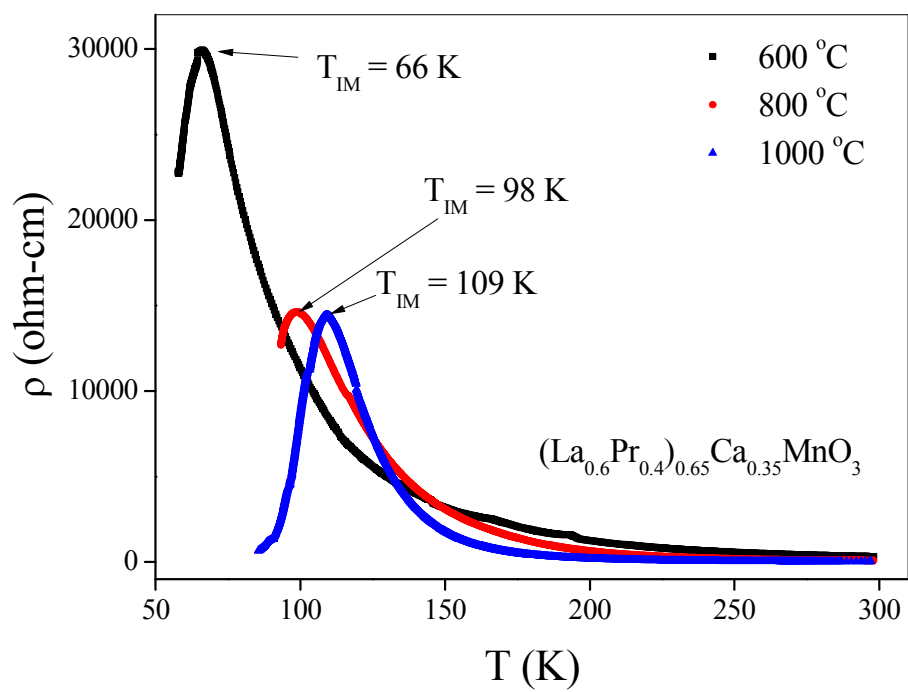
Figure 7
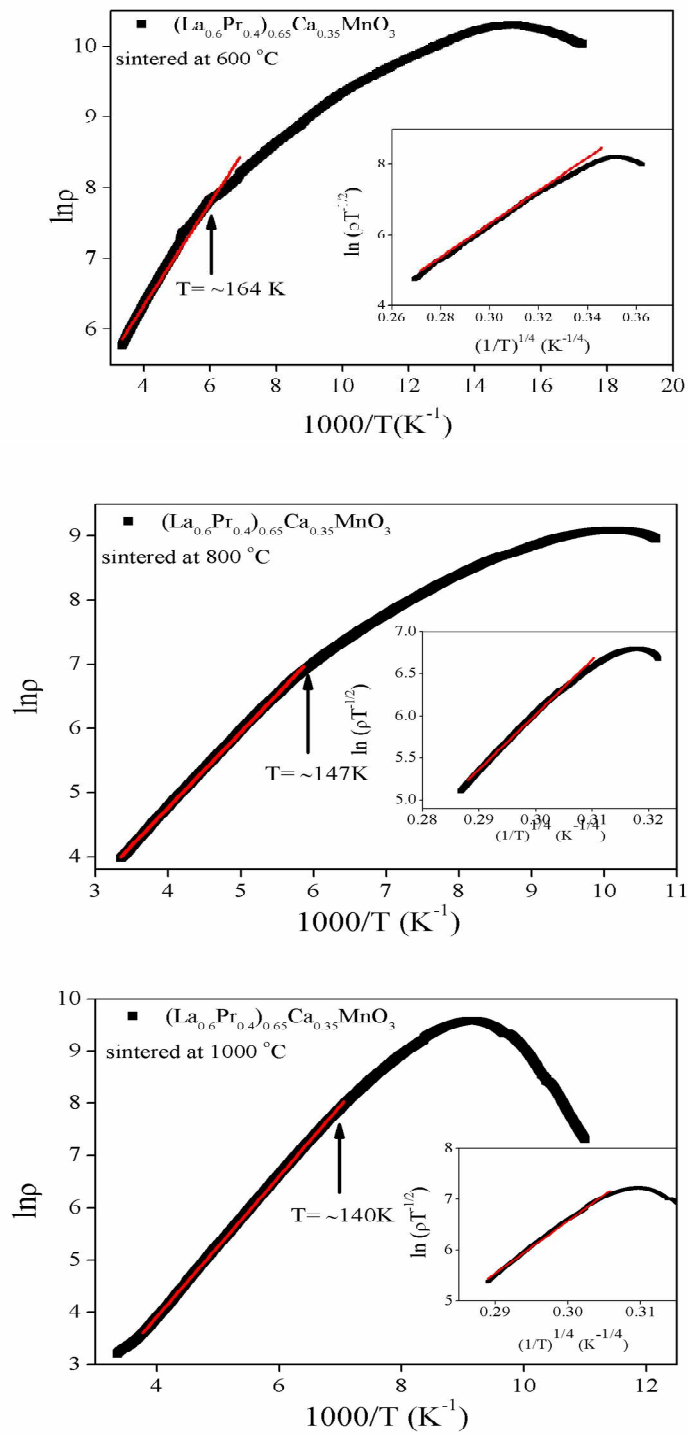
Figure 8

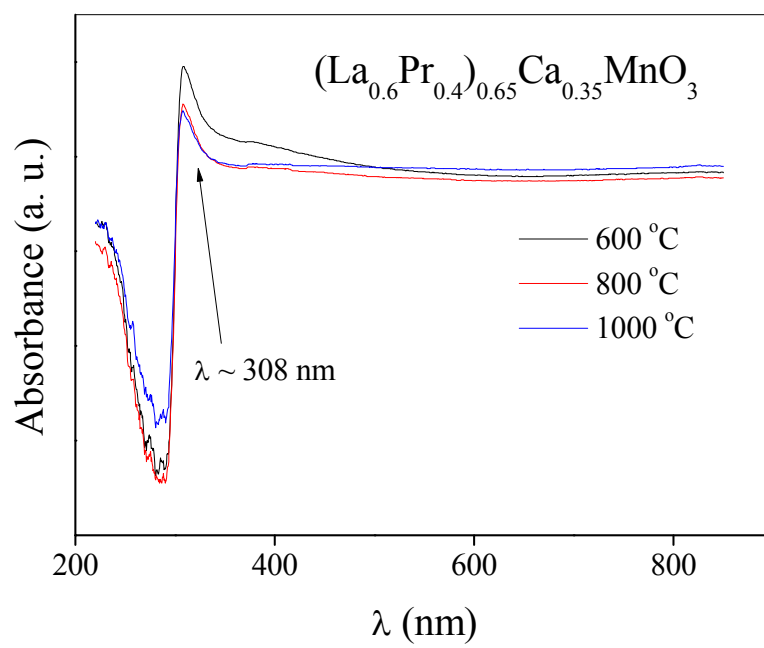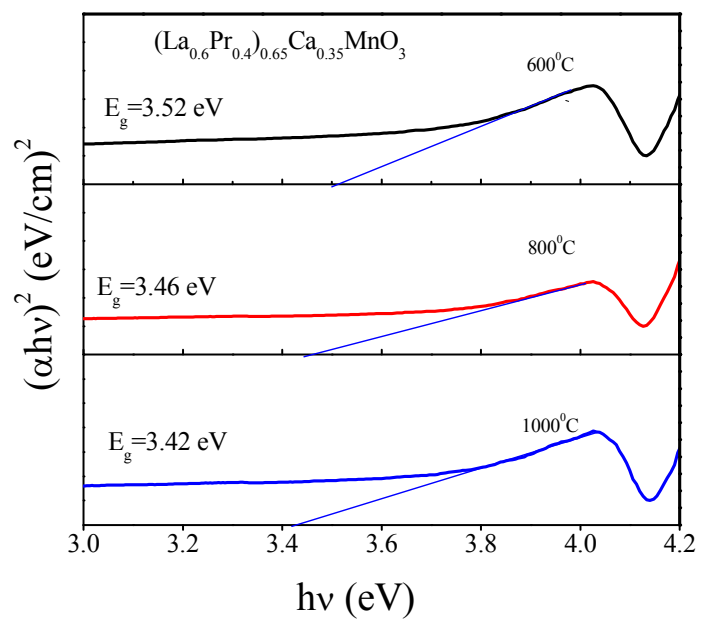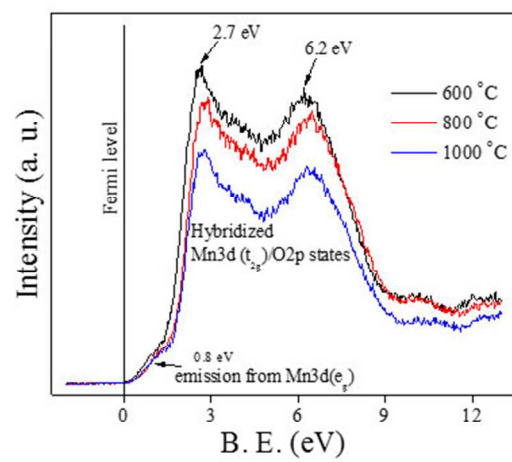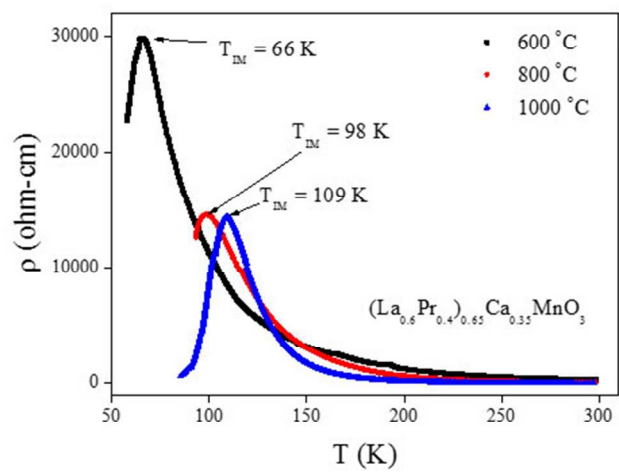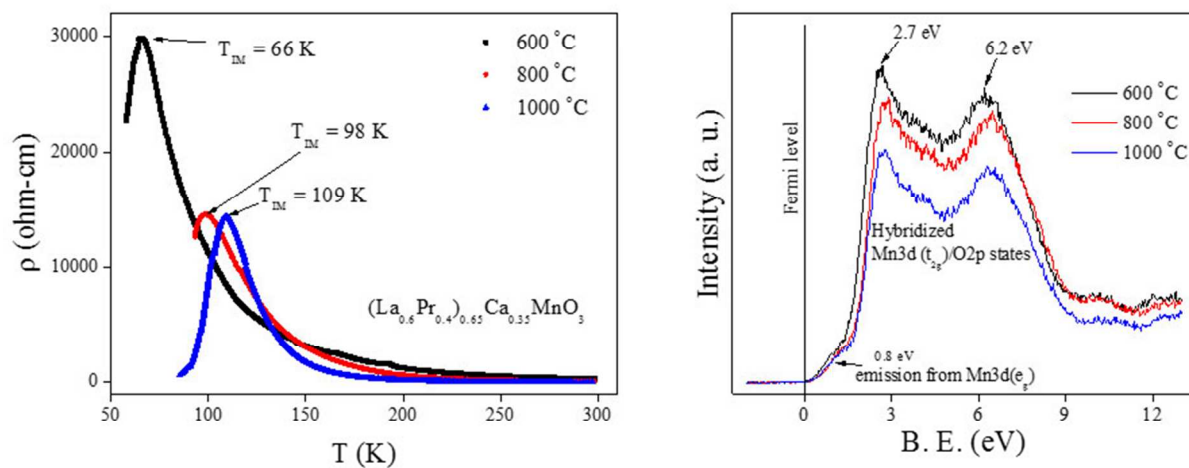Figure 9

Figure 10

Table of Content

Textual and Graphical Abstract

The Figures indicate the variation of resistivity with temperature of $(La_{0.6}Pr_{0.4})_{0.65}Ca_{0.35}MnO_3$ nanoparticles sintered at 600 °C, 800 °C and 1000 °C and Valence band spectra of $(La_{0.6}Pr_{0.4})_{0.65}Ca_{0.35}MnO_3$ nanoparticles sintered at 600 °C, 800 °C and 1000 °C. This figure clearly shows the hybridization of $Mn3d(t_{2g})$ and O2p states.